

Gravitational Lensing of Supernovae Type Ia by Pseudo Elliptic NFW Haloes

Hamed Bagherpour ¹

*Homer L. Dodge Department of Physics and Astronomy, University of Oklahoma,
Norman, OK 73019, USA*

ABSTRACT

We present the effects of ellipticity of matter distribution in massive halos on the observation of supernovae. A pseudo elliptical Navarro-Frenk-White (NFW) mass model is used to calculate the introduced gain factors and observation rates of type Ia supernovae due to the strong lensing. We investigate how and to what extent the ellipticity in mass distribution of the deflecting halos can affect surveys looking for cosmologically distant supernovae. We use halo masses of $1.0 \times 10^{12} h^{-1} M_{\odot}$ and $1.0 \times 10^{14} h^{-1} M_{\odot}$ at redshifts $z_d = 0.2$, $z_d = 0.5$, and $z_d = 1.0$, with ellipticities of up to $\epsilon = 0.2$.

Subject headings: gravitational lensing — supernovae: general

1. Introduction

Supernovae have emerged as the most promising standard candles. Due to their significant intrinsic brightness and relative ubiquity they can be observed in the local and distant universe. Observational efforts to detect high-redshift supernovae have proved their value as cosmological probes. The systematic study and observation of these faint supernovae (mainly type Ia) has been utilized to constrain the cosmic expansion history (Goobar & Perlmutter 1995; Perlmutter et al. 1999; Schmidt et al. 1998). Light emitted from any celestial object is subject to lensing by intervening objects while traversing the large distances involved (Kantowski, Vaughan, & Branch 1995) and the farther the light source, the higher its chance of being significantly lensed. Apart from the fact that gravitational lensing can limit the accuracy of luminosity distance measurements (Perlmutter & Schmidt 2003), it can change the observed rate of supernovae as well.

¹hamed@nhn.ou.edu

Studying supernovae and their rates at high redshifts provide us with much needed information for constraining the measurements of the elusive dark energy, as well as understanding the cosmic star formation rate and metal enrichment at high redshifts. In order to observe and, hence, study the faint high-redshift supernovae, one can raise the chance of observation by looking through clusters of galaxies or even massive galaxies (see Smail, et al. (2002) and the references therein). These ‘gravitational telescopes’ amplify the high-redshift supernovae and thereby increase the chance of their detection. However, this boost in observation is offset by the competing effect of depletion (Fig. 1), due to the field being spread by the deflector (amplification bias). For an assumed lens model and a given field of view it is not obvious which effect dominates the observation of supernovae through the halo. The net result depends on the deflector and source parameters as well as the observational setup (Gunnarsson & Goobar 2003).

Some research has been conducted on the feasibility of observing supernovae through cluster of galaxies (see, for instance, Saini, Raychaudhary, & Shchekinov 2002; Gal-Yam, Maoz, & Sharon 2002; Gunnarsson & Goobar 2003). These studies have not taken into account how the morphology (mainly the ellipticity) of these clusters as gravitational telescopes could change the expected supernova rate. In this paper, we investigate whether introducing ellipticity into the mass distribution of the deflecting halos can affect the observation of supernovae. For this purpose, we use a pseudo elliptical Navarro-Frenk-White (NFW) halo model with different values of ellipticity. Throughout the paper we assume the so-called concordance cosmology where $\Omega_m = 0.3$, $\Omega_\Lambda = 0.7$, and $h_{100} = 0.67$, with $h_{100} = H_0/100 \text{ km s}^{-1}\text{Mpc}^{-1}$. In § 2 we briefly go over the NFW model and show how an analytical formalism for a pseudo elliptical NFW mass profile can be introduced. Strong lensing by thin deflectors as well as the way ellipticity can affect the amplification is explained in § 3. We present and discuss the results of our calculations in § 4.

2. The NFW Halo Model Profile

2.1. NFW Haloes

High resolution N-body numerical simulations (Navarro, Frenk, & White 1995, 1996, 1997) have indicated the existence of a universal density profile for dark matter halos resulting from the generic dissipationless collapse of density fluctuations. This density profile does not (strongly) depend on the mass of halo, on the power spectrum of initial fluctuations, or on the cosmological parameters. These halo models which are formed through hierarchical clustering diverge with $\rho \propto r^{-1}$ near the halo center and behave as $\rho \propto r^{-3}$ in its outer regions. Inside the virial radius, this so-called NFW halo profile appears to be a very good

description of the mass distribution of objects spanning 9 orders of magnitude in mass: ranging from globular clusters to massive galaxy clusters (see Wright & Brainerd (2000) and references therein). The NFW halo model is similar to Hernquist profile (Hernquist 1990) that gives a good description of elliptical galaxy photometry. However, the two models differ significantly at large radii, possibly due to the fact that elliptical galaxies, contrary to the dark halos, are relatively isolated systems.

The spherically symmetric NFW density profile takes the form of

$$\rho(r) = \frac{\delta_c \rho_c}{\frac{r}{r_s} \left(1 + \frac{r}{r_s}\right)^2} \quad (1)$$

where $\rho_c = [3H^2(z)]/(8\pi G)$ is the critical density for closure of the universe at the redshift z of the halo, $H(z)$ is the Hubble parameter at the same redshift, and G is the universal gravity constant. The scale radius $r_s \equiv r_{200}/c$ is the characteristic radius of the halo where c is a dimensionless number referred to as the concentration parameter, and

$$\delta_c = \frac{200}{3} \frac{c^3}{\ln(1+c) - \frac{c}{1+c}} \quad (2)$$

is a characteristic overdensity for the halo. The virial radius r_{200} is defined as the radius inside which the mass density of the halo is equal to $200\rho_c$. It is then easy to see that

$$M(r_{200}) \equiv M_{200} = \frac{800}{3} \rho_c r_{200}^3. \quad (3)$$

Therefore, NFW halos are defined by two parameters; c , and either r_{200} or M_{200} . For any spherical NFW profile with a given mass, the concentration parameter c can be calculated using the Fortran 77 code `charden.f` publicly available on the webpage of Julio Navarro¹.

NFW halos can be shown to always produce odd number of images, as opposed to the commonly-used singular isothermal sphere (SIS) model which produces either one or two images (Schneider, Ehlers, & Falco 1992). Although baryons are expected to isothermalize the matter distribution for halos of galaxy mass and below (Kochanek & White 2001), taking all of the matter in the universe in isothermal spheres is a great oversimplification (Holz 2001). It is, hence, reasonable to model halos (at least massive halos) with NFW mass profile instead of SIS model.

¹<http://pinot.phys.uvic.ca/~jfn/mywebpage/jfn.I.html>

2.2. Elliptical Potential Model

Here we present the introduced ellipticity ϵ in the circular lensing potential $\varphi(\theta)$, assuming that angular position θ can be scaled by some scale radius/angle θ_s . The reader is encouraged to see Golse & Kneib (2002) and Meneghetti, Bartelmann, & Moscardini (2003) for illuminating discussions. We first introduce the dimensionless radial coordinates $\mathbf{x} = (x_1, x_2) = \mathbf{R}/r_s = \theta/\theta_s$ where \mathbf{R} is the radial coordinate in the deflector plane, and $\theta_s = r_s/D_d$. Then, one can introduce the ellipticity in the expression of the lens potential by substituting x_ϵ for x , using the following elliptical coordinate system:

$$\begin{cases} x_{1\epsilon} &= \sqrt{a_{1\epsilon}} x_1 \\ x_{2\epsilon} &= \sqrt{a_{2\epsilon}} x_2 \\ x_\epsilon &= \sqrt{x_{1\epsilon}^2 + x_{2\epsilon}^2} = \sqrt{a_{1\epsilon} x_1^2 + a_{2\epsilon} x_2^2} \\ \phi_\epsilon &= \arctan(x_{2\epsilon}/x_{1\epsilon}) \end{cases} \quad (4)$$

where $a_{1\epsilon}$ and $a_{2\epsilon}$ are the two parameters used to define the ellipticity, as explained below.

From the elliptical lens potential $\varphi_\epsilon(x) \equiv \varphi(x_\epsilon)$, we can calculate the elliptical deflection angle (see § 3.2):

$$\boldsymbol{\alpha}_\epsilon(\mathbf{x}) = \begin{pmatrix} \frac{\partial \varphi_\epsilon}{\partial x_1} = \alpha(x_\epsilon) \sqrt{a_{1\epsilon}} \cos \phi_\epsilon \\ \frac{\partial \varphi_\epsilon}{\partial x_2} = \alpha(x_\epsilon) \sqrt{a_{2\epsilon}} \sin \phi_\epsilon \end{pmatrix} \quad (5)$$

Notice that the expressions above hold for any definition of $a_{1\epsilon}$ and $a_{2\epsilon}$. Here, we follow Golse & Kneib (2002) who, in order to be able to analytically derive the convergence and shear, chose the following elliptical parameters:

$$a_{1\epsilon} = 1 - \epsilon \quad (6)$$

$$a_{2\epsilon} = 1 + \epsilon \quad (7)$$

which for small values of ellipticity ϵ results in the same ellipticity along the x_1 as the standard elliptical model of

$$a_{1\epsilon} = 1 - \epsilon \quad (8)$$

$$a_{2\epsilon} = 1/(1 - \epsilon) \quad (9)$$

with $\epsilon = 1 - b/a$, where a and b are the semi-major and semi-minor axis of the projected elliptic potential, respectively.

3. Gravitational Lensing: a Reminder

3.1. General Formalism

In the thin-lens approximation, we define \mathfrak{z} as the optical axis and $\Phi(R, \mathfrak{z})$ as the 3-dimensional Newtonian potential, with $r = \sqrt{R^2 + \mathfrak{z}^2}$. The so-called reduced 2-dimensional potential which is defined in the deflector plane is given by

$$\varphi(\theta) = \frac{2}{\mathfrak{c}^2} \frac{D_{ds}}{D_d D_s} \int_{-\infty}^{+\infty} \Phi(D_d \theta, \mathfrak{z}) d\mathfrak{z} \quad (10)$$

(Schneider, Ehlers, & Falco 1992) where \mathfrak{c} is the speed of light, and $\theta = (\theta_1, \theta_2)$ is the angular position in the image plane. D_d , D_s , and D_{ds} are angular distances of observer-deflector, observer-source, and deflector-source, respectively. The deflection angle α , convergence κ and the shear γ are given by the following set of equations:

$$\begin{cases} \boldsymbol{\alpha}(\theta) = \nabla_{\theta} \varphi(\theta) \\ \kappa(\theta) = \frac{1}{2} \left(\frac{\partial^2 \varphi}{\partial \theta_1^2} + \frac{\partial^2 \varphi}{\partial \theta_2^2} \right) \\ \gamma^2(\theta) = \|\gamma(\theta)\|^2 = \frac{1}{4} \left(\frac{\partial^2 \varphi}{\partial \theta_1^2} - \frac{\partial^2 \varphi}{\partial \theta_2^2} \right)^2 + \left(\frac{\partial^2 \varphi}{\partial \theta_1 \partial \theta_2} \right)^2. \end{cases} \quad (11)$$

The lensing equation then reads:

$$\beta = \theta - \alpha = \theta - \nabla_{\theta} \varphi(\theta) \quad (12)$$

where $\beta = (\beta_1, \beta_2)$ is the angular location of the source. The amplification amp of a point image formed at θ is:

$$amp(\theta) = \frac{1}{(1 - \kappa)^2 - \gamma^2} \quad (13)$$

To calculate the angular distances in our work, we use the solution to the Lamé equation for the distance-redshift equation in a partially filled beam Friedmann-Lemaître-Robertson-Walker (FLRW) cosmology. For a filled-beam flat FLRW cosmology, the angular distance D as a function of redshift z is

$$D(z) = \frac{2\mathfrak{c}z}{(1+z)H_0 (g(z))^{1/2}} {}_2F_1 \left(\frac{1}{6}, \frac{1}{2}; \frac{7}{6}, - \left[\frac{(\Omega_m^2 \Omega_{\Lambda})^{1/3} z^2}{g(z)} \right]^3 \right) \quad (14)$$

where

$$g(z) \equiv 2\sqrt{1 + \Omega_m z(3 + 3z + z^2)} + 2 + \Omega_m z(3 + z). \quad (15)$$

See Kantowski (2003) for more detail.

3.2. Lensing Parameters of Spherically symmetric NFW Model

Several authors have developed the lensing equations for the ordinary, spherical NFW halos (e.g. Bartelmann 1996; Wright & Brainerd 2000; Golse & Kneib 2002). Following § 2.2 we can introduce a dimensionless radial coordinate in the lens plane $\mathbf{x} = (x_1, x_2) = \mathbf{R}/r_s = \theta/\theta_s$ where $\theta_s = r_s/D_d$. The surface mass density then becomes

$$\Sigma(x) = \int_{-\infty}^{+\infty} \rho(r_s x, z) dz = 2\delta_c \rho_c r_s F(x) \quad (16)$$

with

$$F(x) = \begin{cases} \frac{1}{x^2 - 1} \left(1 - \frac{1}{\sqrt{1 - x^2}} \operatorname{arccch} \frac{1}{x} \right) & (x < 1) \\ \frac{1}{3} & (x = 1) \\ \frac{1}{x^2 - 1} \left(1 - \frac{1}{\sqrt{x^2 - 1}} \arccos \frac{1}{x} \right) & (x > 1) \end{cases} \quad (17)$$

and the mean surface density inside the radius x can be written as

$$\bar{\Sigma}(x) = \frac{1}{\pi x^2} \int_0^x 2\pi x \Sigma(x) dx = 4\delta_c \rho_c r_s \frac{g(x)}{x^2} \quad (18)$$

with

$$g(x) = \begin{cases} \ln \frac{x}{2} + \frac{1}{\sqrt{1 - x^2}} \operatorname{arccch} \frac{1}{x} & (x < 1) \\ 1 + \ln \frac{1}{2} & (x = 1) \\ \ln \frac{x}{2} + \frac{1}{\sqrt{x^2 - 1}} \arccos \frac{1}{x} & (x > 1) \end{cases} \quad (19)$$

(see Golse & Kneib (2002)).

The deflection angle α , convergence κ and shear γ turn out as

$$\begin{cases} \alpha(x) = \theta \frac{\bar{\Sigma}(x)}{\Sigma_{\text{crit}}} = 4\kappa_s \frac{\theta}{x^2} g(x) \mathbf{e}_x \\ \kappa(x) = \frac{\bar{\Sigma}(x)}{\Sigma_{\text{crit}}} = 2\kappa_s F(x) \\ \gamma(x) = \frac{\bar{\Sigma}(x) - \Sigma(x)}{\Sigma_{\text{crit}}} = 2\kappa_s \left(\frac{2g(x)}{x^2} - F(x) \right) \end{cases} \quad (20)$$

where $\kappa_s = \delta_c \rho_c r_s \Sigma_{\text{crit}}^{-1}$, with $\Sigma_{\text{crit}} \equiv c^2 D_s / (4\pi G D_d D_{ds})$.

By integrating the deflection angle, the potential $\varphi(x)$ can be found:

$$\varphi(x) = 2\kappa_s\theta_s^2 h(x) \quad (21)$$

with

$$h(x) = \begin{cases} \ln^2 \frac{x}{2} - \operatorname{arcch}^2 \frac{1}{x} & (x < 1) \\ \ln^2 \frac{x}{2} + \operatorname{arccos}^2 \frac{1}{x} & (x \geq 1) \end{cases} \quad (22)$$

3.3. Lensing Parameters of Pseudo Elliptical NFW Model

For the particular choice of ϵ in § 2.2, the corresponding convergence and shear can be calculated:

$$\begin{aligned} \kappa_\epsilon(x) &= \frac{1}{2\theta_s^2} \left(\frac{\partial^2 \varphi_\epsilon}{\partial x_1^2} + \frac{\partial^2 \varphi_\epsilon}{\partial x_2^2} \right) \\ &= \kappa(x_\epsilon) + \frac{\epsilon}{2\theta_s^2} \left(\frac{\partial^2 \varphi(x_\epsilon)}{\partial x_{2\epsilon}^2} - \frac{\partial^2 \varphi(x_\epsilon)}{\partial x_{1\epsilon}^2} \right) \\ &= \kappa(x_\epsilon) + \epsilon \cos 2\phi_\epsilon \gamma(x_\epsilon). \end{aligned} \quad (23)$$

and

$$\begin{aligned} \gamma_\epsilon^2(x) &= \frac{1}{4\theta_s^4} \left\{ \left(\frac{\partial^2 \varphi_\epsilon}{\partial x_1^2} - \frac{\partial^2 \varphi_\epsilon}{\partial x_2^2} \right)^2 + \left(2 \frac{\partial^2 \varphi_\epsilon}{\partial x_1 \partial x_2} \right)^2 \right\} \\ &= \gamma^2(x_\epsilon) + 2\epsilon \cos 2\phi_\epsilon \gamma(\vec{x}_\epsilon) \kappa(x_\epsilon) + \epsilon^2 (\kappa^2(x_\epsilon) - \cos^2 2\phi_\epsilon \gamma^2(x_\epsilon)). \end{aligned} \quad (24)$$

Also, the elliptic projected mass density reads:

$$\Sigma_\epsilon(\mathbf{x}) = \Sigma(\mathbf{x}_\epsilon) + \epsilon \cos 2\phi_\epsilon (\bar{\Sigma}(\mathbf{x}_\epsilon) - \Sigma(\mathbf{x}_\epsilon)). \quad (25)$$

The lensing equation now becomes (see the appendix):

$$\begin{cases} \beta_1 &= \theta_s x_1 \left(1 - 4k_s \epsilon_1 \frac{g(x_\epsilon)}{x_\epsilon^2} \right) \\ \beta_2 &= \theta_s x_2 \left(1 - 4k_s \epsilon_2 \frac{g(x_\epsilon)}{x_\epsilon^2} \right) \end{cases} \quad (26)$$

and as one expects, the amplification amp reads:

$$amp(\mathbf{x}) = \frac{1}{(1 - \kappa_\epsilon(\mathbf{x}))^2 - \gamma_\epsilon^2(\mathbf{x})} \quad (27)$$

It can be shown that ellipticities beyond $\epsilon = 0.2$ result in unrealistic ‘peanut’ shaped projected densities, hence in this work we focus on lower values of ϵ . Figure 2 shows the multiple images produced by a $1.0 \times 10^{14} h^{-1} M_{\odot}$ halo with ellipticity $\epsilon = 0.1$ (courtesy of Golse & Kneib). Dashed lines are the contours with constant surface density Σ_{ϵ} and the solid lines are the critical and caustic lines. Redshifts of source and deflector are 0.2 and 1.0, respectively.

4. The Method

The main reason for studying supernovae magnified by gravitational lensing is to investigate the chance of observing supernovae too faint to be observed in the absence of lensing, which is usually the case for cosmologically distant supernovae, specifically type Ia’s. To calculate the observed rate of type Ia supernovae we use the result of predicted rates by Dahlén & Fransson (1999) for a hierarchical star formation rate model with a characteristic time of $\tau = 1$ Gyr (Fig. 3), which limits our calculation to the redshift depth of $z_{Max} = 5$.

In order for a supernova to be detected, its apparent magnitude m should not exceed the limiting magnitude of the survey m_{limit} . Using the definitions of the apparent magnitude and amplification, we get:

$$m_{amp} = m_o + 2.5 \log(|(1 - \kappa)^2 - \gamma^2|) \quad (28)$$

in which, m_{amp} is the observed magnitude, and m_o is the apparent magnitude of the supernova in the absence of the lensing. We can further write m_o in terms of the absolute magnitude M_{abs} of the supernova and rewrite the detection criterion as

$$((1 - \kappa)^2 - \gamma^2) D_L^2(z_s) \leq 10^{\left(\frac{m_{limit} - M_{abs} + 5}{2.5}\right)} \quad (29)$$

where $D_L(z_s)$ is the luminosity distance of the supernova at redshift z_s . The absolute magnitude of type Ia SNe has a very narrow Gaussian distribution around $M_{abs} = -19.16$ at a confidence level of 89% (Richardson et al. 2002). Here, we assume that the supernova is detected as soon as its absolute magnitude becomes brighter than $M_{abs} = -18$.

We take the deflecting halo to be at redshifts $z_s = 0.2, 0.5,$ and 1.0 , and with virial masses of $m_{d1} = 1.0 \times 10^{12} h^{-1} M_{\odot}$ and $m_{d2} = 1.0 \times 10^{14} M_{\odot} h^{-1}$. Concentration parameter c , overdensity δ_c , and virial radius r_{200} (in units of $Kpch^{-1}$) for each case are given in Table 1.

The field of view is taken to be the spatial angle subtending the virial area of the halo. By breaking the projected halo into pixels with the angular size of δx_1 and δx_2 (which are taken to be smaller than the angular resolution of the observation, Figure 4), we calculate

the amplification across the halo and hence, find the number of observable supernovae in redshift shells with the width of $\delta z = 0.05$. We find the corresponding (spatial angular) element $\delta\beta_1 \times \delta\beta_2$ in the area behind the halo (in redshift space) where the supernovae are bright enough to be detected. Assuming we can arbitrarily minimize δx_1 and δx_2 , we have

$$\delta\beta_1 \times \delta\beta_2 = \left| \frac{\partial\beta}{\partial\mathbf{x}} \right| \delta x_1 \times \delta x_2 \quad (30)$$

where $\left| \frac{\partial\beta}{\partial\mathbf{x}} \right|$ is the determinant of Jaccobian matrix.

The reader can refer to the appendix for the derivation of the Jaccobian. The gain factor, defined as the ratio of the number of observable lensed supernovae over the number of observable supernovae in the absence of lensing ($N_{lensed}/N_{NoLensing}$) can be calculated by integrating over the predicted rates of both cases across the whole observable area (Fig. 1) for any given lensing configuration, considering the ellipticity ϵ .

5. Results and Discussion

First, we consider the effect of ellipticity in the number rate of SN Ia in every redshift bin $\delta z = 0.05$. Upper panels of Figures 5 (m_{d1}) and 6 (m_{d2}) show the number of expected supernovae per year occuring in the redshift bins. We present the results for $\epsilon = 0.0$ and $\epsilon = 0.2$ with the deflecting halo at redshifts $z_d = 0.2, 0.5, \text{ and } 1.0$. The survey magnitude is assumed to be $m_{lim} = 27$. The number rate peaks at around $z = 1.3$ as expected (see Fig. 3) and dies off rapidly beyond that. It can be seen that the farther the deflector, the slightly higher the slope of the curves up to $z = 1.3$ as a result of higher number of supernovae observed in front of the deflector.

Middle and lower panels in Figures 5 and 6 show the cumulative number rates and the gains, respectively. The dominance of amplification bias as a result of the narrowing of the

m_d	$1.0 \times 10^{12} h^{-1} M_\odot$			$1.0 \times 10^{14} h^{-1} M_\odot$		
z_d	r₂₀₀	δ_c	c	r₂₀₀	δ_c	c
0.2	152.61	38468.6	9.40	708.36	15741.7	6.46
0.5	136.24	33096.0	8.83	632.38	14426.7	6.22
1.0	111.79	25118.2	7.87	518.88	12086.5	5.77

Table 1: NFW halo parameters for the two halo masses m_d at the given redshifts z_d used in the paper.

field in a region immediately behind the deflectors at the assumed redshifts is clear, as the gains fall below 1. Beyond that region amplification takes over and more (lensed) supernovae are observed.

In the absence of an intercepting halo, the number rate of the survey drops to zero at the redshift limit of the survey. With the deflecting halo present, the observed rate goes to zero at a higher redshift. This can be seen in figures 7 (m_{d1}) and 8 (m_{d2}) where the deflector is at redshift $z_d = 0.5$ and the survey magnitude limit is $m_{lim} = 27$. The three upper panels depict the expected rates for lensing and no-lensing scenarios for ellipticities $\epsilon = 0.0, 0.1,$ and 0.2 . The number rates per redshift bin (left) and the cumulative rate (right) are given. The reader can readily notice the effect of bias behind the halo. With the galactic size halo m_{d1} , the survey can detect supernovae up to redshift $z \sim 3$ (Fig. 7). This limit increases to $z \sim 5$ (Fig. 8) for the cluster-size halo m_{d2} .

The lowest panel in these two figures show the relative difference of the cases with $\epsilon = 0.1$ and $\epsilon = 0.2$ with respect to $\epsilon = 0.0$. The 2 curves do not show significant difference for the redshift bins in front of the halo. In the regime behind the halo, the difference becomes remarkable: it increases up to redshift $z = 1.4$ for m_{d1} and $z = 1.7$ for m_{d2} . The difference doesn't vary remarkably beyond the maximum point.

To further see how ellipticity changes the expected rate of observed supernovae we put the result of our calculations for different ellipticities for a given range of magnitude limits on the same plot. Figure 9 shows the number rate of observed type Ia supernovae (upper panel) for ellipticities $\epsilon = 0.1$ and $\epsilon = 0.2$ together with their relative difference with respect to the case with no ellipticity (lower panel). Both halo masses, m_{d1} and m_{d2} are at redshift $z_d = 0.2$. Figures 10 and 11 show the results of the same calculations with halos at redshifts $z = 0.5$ and $z = 1.0$, respectively. The number rates in each figure increase smoothly up to the magnitude limit at which the survey is deep enough to detect the supernovae as far as the halo itself, e.g, $m_{lim} = 22.4$ for a concordance cosmology of $(\Omega_m, \omega_\Lambda, h_{100}) = (0.3, 0.7, 0.67)$. From that point on the rates increase very rapidly as the magnitude limit goes up. That is caused by the halo lensing and hence amplifying the supernovae which would otherwise be too dim to be observed. The relative differences depicted in these figures show that even at a magnitude limit of 25, effect of ellipticity cannot be ignored as it significantly changes the number/percentage of the observed supernovae; for instance, the relative difference for $\epsilon = 0.2$ with deflecting halo m_{d2} at redshift $z = 1.0$ (Fig. 11) exceeds 9% for the magnitude limit of $m_{lim} = 27$.

6. Conclusion

Aiming behind massive halos seem to be a good way to enhance the high-redshift supernovae surveys. The cumulative gains of such surveys seem insignificant at low redshifts ($z_s < 0.2$) but the results are remarkable at higher redshifts. For deep observations where $m_{lim} > 25$, the geometry of the intervening halo cannot be ignored. We have shown that introducing ellipticity in the (gravitational potential of) the mass distribution of a deflecting halo (here, for a galactic halo of mass $1.0 \times 10^{12} M_\odot h^{-1}$ as well as a middle-size cluster of galaxies with a mass of $1.0 \times 10^{14} M_\odot h^{-1}$) can affect the rate of observed supernovae by a few percent. It was shown that the farther the supernova survey probes, the more significant the effects of introduced ellipticity become.

It should be noted that this work does not involve a broad range of mass profiles for the halos (although we specify that the survey is limited to the virial area of the halo), nor does it address the much needed k-correction. Our calculations are actually an oversimplification due to the fact that a large, massive halo like a galaxy cluster has substructure which consists of the member galaxies, as well as large clouds of gas. A more sophisticated lens model with ellipticity should be employed to calculate the number rate of observed supernovae.

The author wishes to thank D. Branch for enlightening discussions and suggestions. The author would also like to thank C. Gunnarsson and A. Goobar for generously offering him their data set on the rate of SNe Ia, and J. Navarro for allowing him to use the NFW code. This work was in part supported by NSF grant AST0204771 and NASA grant NNG04GD36G.

A. Appendix

Here we derive the lensing equation for an elliptical NFW halo with ellipticity of ϵ introduced in its 2-dimensional potential, and proceed to calculate Jaccobian $\frac{\partial \beta}{\partial \mathbf{x}}$ needed to get the spatial angular element $\delta\beta_1 \times \delta\beta_2$ in the source frame.

Lensing Equation

Introducing the dimensionless coordinate system $\mathbf{x} = (x_1, x_2) = \mathbf{R}/r_s = \theta/\theta_s$, the lensing equation becomes

$$\begin{cases} \beta_1 &= \theta_s x_1 - \alpha_1 [x_1, x_2] \\ \beta_2 &= \theta_s x_2 - \alpha_2 [x_1, x_2] \end{cases} \quad (\text{A1})$$

Given the elliptical deflection angle of

$$\alpha_\epsilon(\mathbf{x}) = \begin{pmatrix} \frac{\partial\varphi_\epsilon}{\partial x_1} = \alpha(x_\epsilon)\sqrt{a_{1\epsilon}} \cos \phi_\epsilon \\ \frac{\partial\varphi_\epsilon}{\partial x_2} = \alpha(x_\epsilon)\sqrt{a_{2\epsilon}} \sin \phi_\epsilon \end{pmatrix} \quad (\text{A2})$$

and the deflection angle of α as

$$\boldsymbol{\alpha}(x) = \theta \frac{\bar{\Sigma}(x)}{\Sigma_{\text{crit}}} = 4\kappa_s \frac{\theta}{x^2} g(x) \mathbf{e}_x \quad (\text{A3})$$

the lensing equation now reads

$$\begin{cases} \beta_1 = \theta_s x_1 \left(1 - 4k_s \epsilon_1 \frac{g(x_\epsilon)}{x_\epsilon^2} \right) \\ \beta_2 = \theta_s x_2 \left(1 - 4k_s \epsilon_2 \frac{g(x_\epsilon)}{x_\epsilon^2} \right) \end{cases} \quad (\text{A4})$$

Jacobian

To calculate spatial angular element $\delta\beta_1 \times \delta\beta_2$ we use the Jacobian equation

$$\delta\beta_1 \times \delta\beta_2 = \left| \frac{\partial\boldsymbol{\beta}}{\partial\mathbf{x}} \right| \delta x_1 \times \delta x_2 = \left| \frac{\partial\beta_1}{\partial x_1} \cdot \frac{\partial\beta_2}{\partial x_2} - \frac{\partial\beta_1}{\partial x_2} \cdot \frac{\partial\beta_2}{\partial x_1} \right| \delta x_1 \times \delta x_2 \quad (\text{A5})$$

Given Eq. A4, we get:

$$\begin{cases} \frac{\partial\beta_1}{\partial x_1} = \theta_s (1 - 4k_s a_{1\epsilon} G(x_\epsilon)) \theta_s x_1 \left(1 - 4k_s a_{1\epsilon} \frac{\partial G(x_\epsilon)}{\partial x_1} \right) \\ \frac{\partial\beta_2}{\partial x_1} = \theta_s x_2 \left(1 - 4k_s a_{2\epsilon} \frac{\partial G(x_\epsilon)}{\partial x_1} \right) \\ \frac{\partial\beta_1}{\partial x_2} = \theta_s x_1 \left(1 - 4k_s a_{1\epsilon} \frac{\partial G(x_\epsilon)}{\partial x_2} \right) \\ \frac{\partial\beta_2}{\partial x_2} = \theta_s (1 - 4k_s a_{2\epsilon} G(x_\epsilon)) \theta_s x_2 \left(1 - 4k_s a_{2\epsilon} \frac{\partial G(x_\epsilon)}{\partial x_2} \right) \end{cases} \quad (\text{A6})$$

where function G is defined as

$$G(x_\epsilon) \equiv \frac{g(x_\epsilon)}{x_\epsilon^2} \quad (\text{A7})$$

and

$$\frac{g(x_\epsilon)}{x_\epsilon^2} = \begin{cases} \frac{x_\epsilon}{(1-x_\epsilon^2)^{\frac{3}{2}}} \operatorname{arccch} \frac{1}{x_\epsilon} - \frac{(1+x_\epsilon^2)}{2x_\epsilon(1-x_\epsilon^2)} & (x_\epsilon < 1) \\ -\frac{1}{6} & (x_\epsilon = 1) \\ \frac{(1+x_\epsilon^2)}{2x_\epsilon(1-x_\epsilon^2)} - \frac{x_\epsilon}{(1-x_\epsilon^2)^{\frac{3}{2}}} \operatorname{arccos} \frac{1}{x_\epsilon} & (x_\epsilon > 1). \end{cases} \quad (\text{A8})$$

REFERENCES

- Bartelmann, M. 1996, *A&A*, 313, 697
- Dahlén, T., & Fransson, C. 1999, *A&A*, 350, 349
- Gal-Yam, A., Maoz, D., & Sharon, K. 2002, *MNRAS*, 332, 37
- Golse, G., & Kneib, J. P. 2002, *A&A*, 390, 821
- Goobar, A., & Perlmutter, S. 1995, *ApJ*, 450, 14
- Gunnarsson, C., & Goobar, A. 2003, *A&A*, 405, 859
- Hernquist, L. 1990, *ApJ*, 356, 359
- Holz, D. 2001, *ApJ*, L71, 2001
- Kantowski, R., Vaughan, T., & Branch, D. 1995, *ApJ*, 447, 35
- Kantowski, R. 2003, *Phys. Rev. D*, 68, 123516
- Kochanek, C. S., & White, M. 2001, *ApJ*, 559, 531
- Meneghetti, M., Bartelmann, M., & Moscardini L. 2003, *MNRAS*, 340, 105
- Navarro, J. F., Frenk, C.S., & White, S. D. M. 1995, *MNRAS*, 275, 720
- Navarro, J. F., Frenk, C.S., & White, S. D. M. 1996, *ApJ*, 462, 563
- Navarro, J. F., Frenk, C.S., & White, S. D. M. 1997, *ApJ*, 490, 493
- Perlmutter, S., et al. 1999, *ApJ*, 517, 565
- Perlmutter, S., & Schmidt B. P. 2003, *Lecture Notes in Physics*, ed. K. Weiler (Berlin: Springer-Verlag)
- Richardson, D., et al. 2002, *AJ*, 123, 745
- Schmidt, B. P., et al. 1998, *ApJ*, 507, 46
- Schneider, P., Ehlers, J., & Falco, E. E. 1992, *Gravitational Lenses* (Berlin: Springer-Verlag)
- Saini, T. D., Raychaudhary, S., & Shchekinov, Y. A. 2000, *A&A*, 363, 349
- Smail, I., et al. 2002, *MNRAS*, 331, 495

Sullivan, M., et al. 2000, MNRAS, 319, 549

Wright, C. O., & Brainerd, T. G. 2000, ApJ, 534, 34

Fig. 1.—

Schematic picture of the lensing configuration by a deflecting halo. z_{halo} is the redshift of the halo and z_{limit} is the redshift corresponding to the limiting magnitude m_{limit} . The shaded area shows the volume where SNe are bright enough to be observed.

Fig. 2.—

Multiple images produced by a $1.0 \times 10^{14} h^{-1} M_{\odot}$ halo with ellipticity $\epsilon = 0.1$. Dashed lines are the contours with constant surface density and the solid lines are the critical and caustic lines. Redshifts of source and deflector are 0.2 and 1.0, respectively (courtesy of Golse & Kneib).

Fig. 3.—

Rates of type Ia supernovae in intervals of $\delta z = 0.05$. Dilution factor of $1 + z$ is taken into account (courtesy of Gunnarsson & Goobar).

Fig. 4.—

This figure shows how the projected deflector is ‘pixellated’ in order to calculate the observable area behind the halo. Each pixel has dimensions of $\delta\omega \times \delta\omega$ with $\delta\omega$ being smaller than the angular resolution of the observation.

Fig. 5.—

Rates of observed supernovae Ia per redshift bin $\delta_z = 0.05$ (upper panel), cumulative rate (middle panel), and the lensing gain (lower panel) for a deflecting halo of mass $m_d = 1.0 \times 10^{12} h^{-1} M_{\odot}$ at redshifts of $z_d = 0.2, 0.5,$ and 1.0 with ellipticities $\epsilon = 0.1$ and 0.2 .

Fig. 6.—

Same as Figure 5, with $m_d = 1.0 \times 10^{14} M_{\odot} h^{-1}$.

Fig. 7.—

In this picture the 3 upper panels show observed rates of lensed (solid line) and unlensed (dash line) for three different ellipticities $\epsilon = 0.0, 0.1,$ and 0.2 . The deflecting halo has a mass of $m_d = 1.0 \times 10^{12} h^{-1} M_{\odot}$ and is located at redshift $z_s = 0.5$. The lowermost panel depicts the relative difference of $\epsilon = 0.1$ (solid line) and $\epsilon = 0.2$ (dash line) with respect to $\epsilon = 0.0$.

Fig. 8.—

Same as Figure 7, with $m_d = 1.0 \times 10^{14} M_{\odot} h^{-1}$.

Fig. 9.—

Rates of observed supernovae Ia as a function of survey magnitude limit m (upper panel). Results are shown for halo masses $m_d = 1.0 \times 10^{12} h^{-1} M_\odot$ and $m_d = 1.0 \times 10^{14} h^{-1} M_\odot$ with ellipticities $\epsilon = 0.1$ and 0.2 . The halo is at redshift $z_d = 0.2$. The relative difference of cases with $\epsilon = 0.1$ and 0.2 with respect to $\epsilon = 0.0$ is given in the lower panel.

Fig. 10.—

Same as Fig. 9 with $z_d = 0.5$.

Fig. 11.—

Same as Fig. 9 with $z_d = 1.0$.

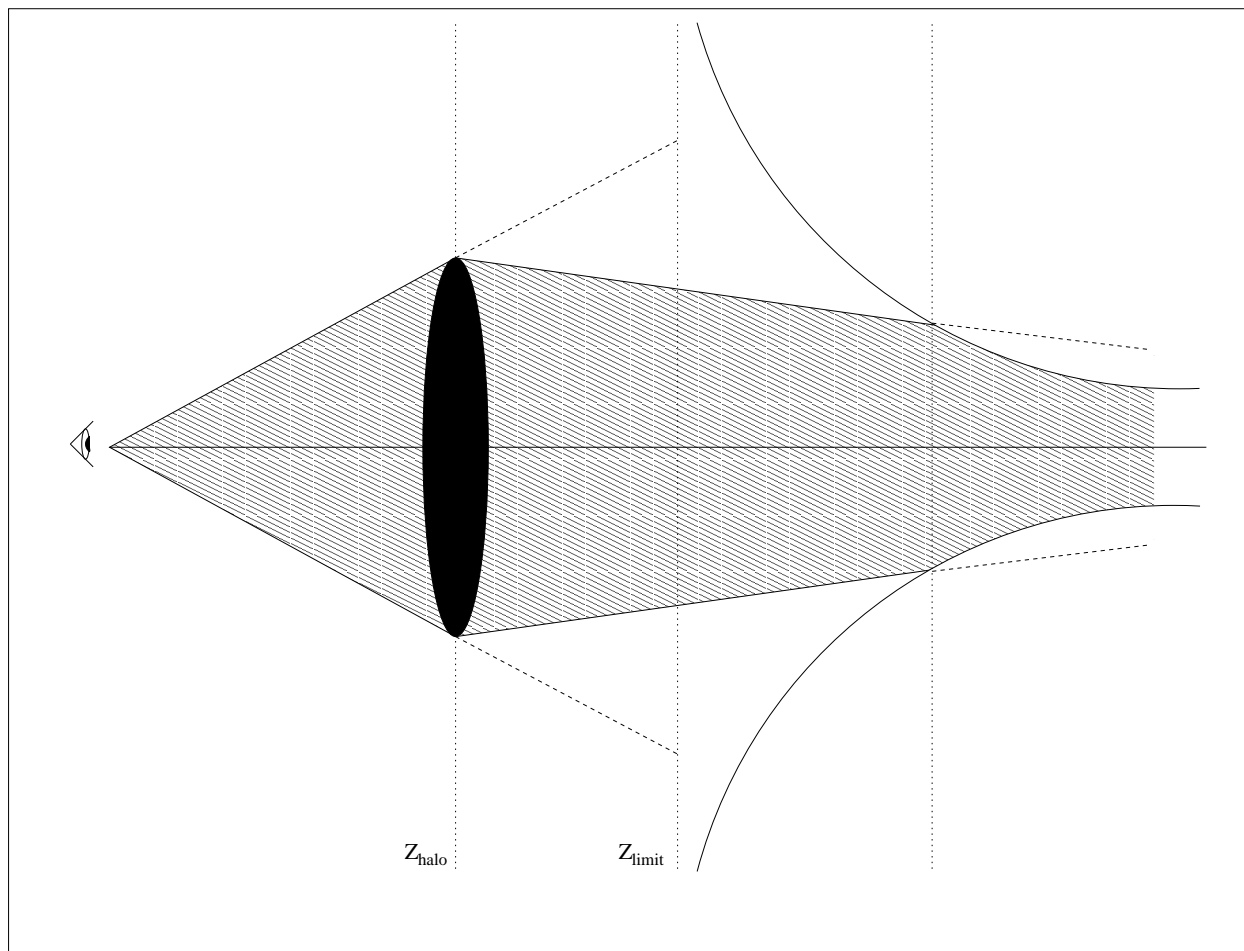


Figure 1

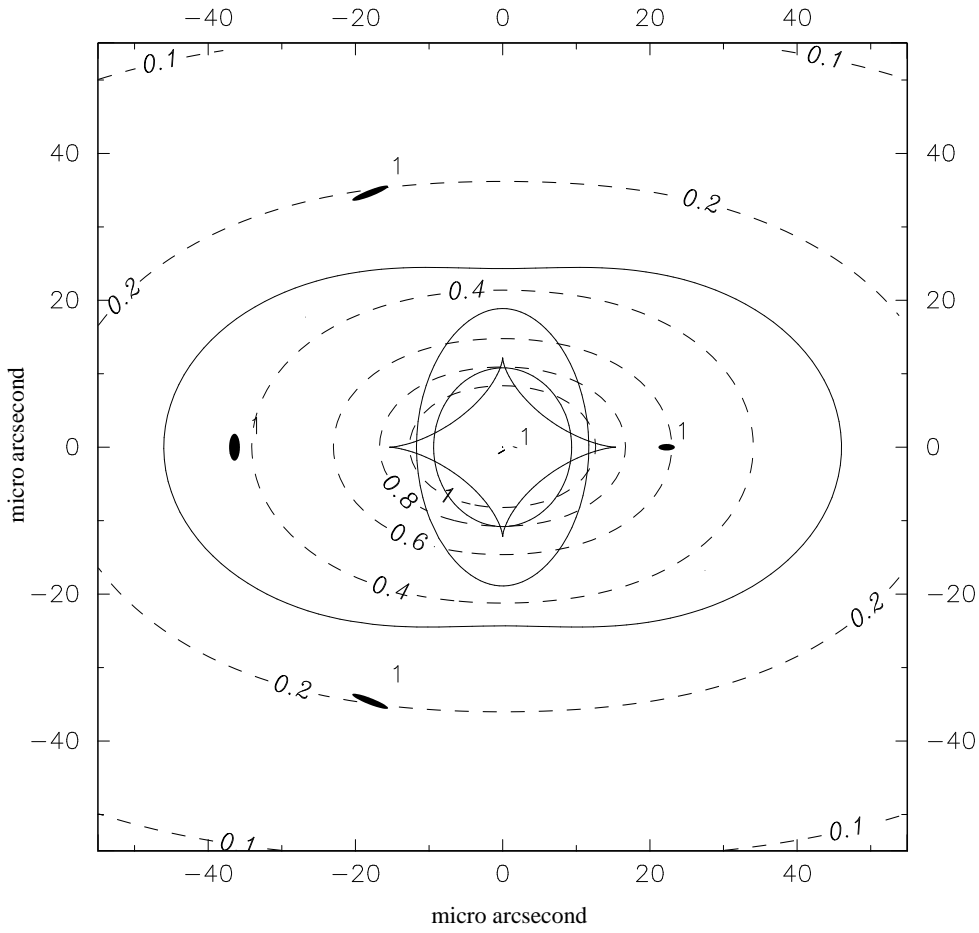


Figure 2

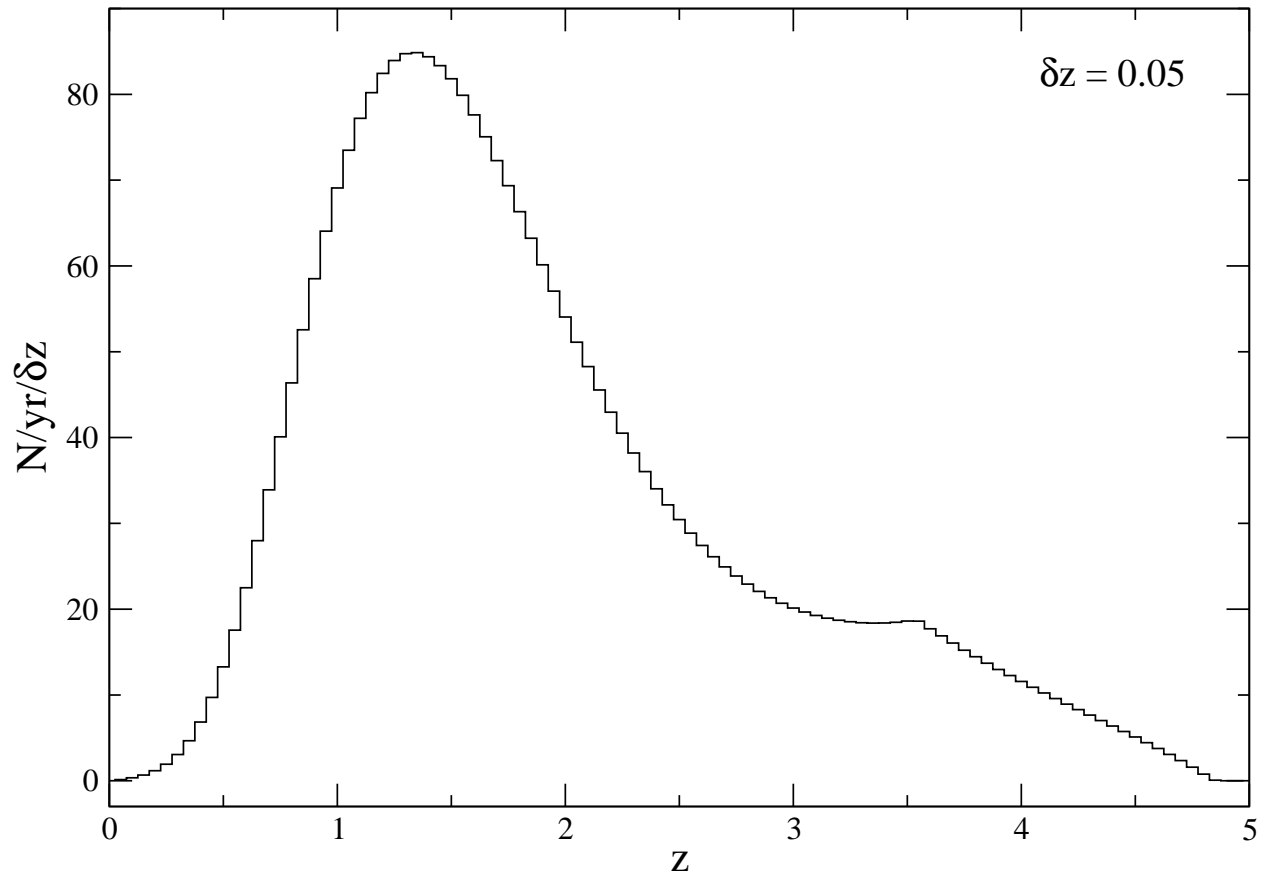


Figure 3

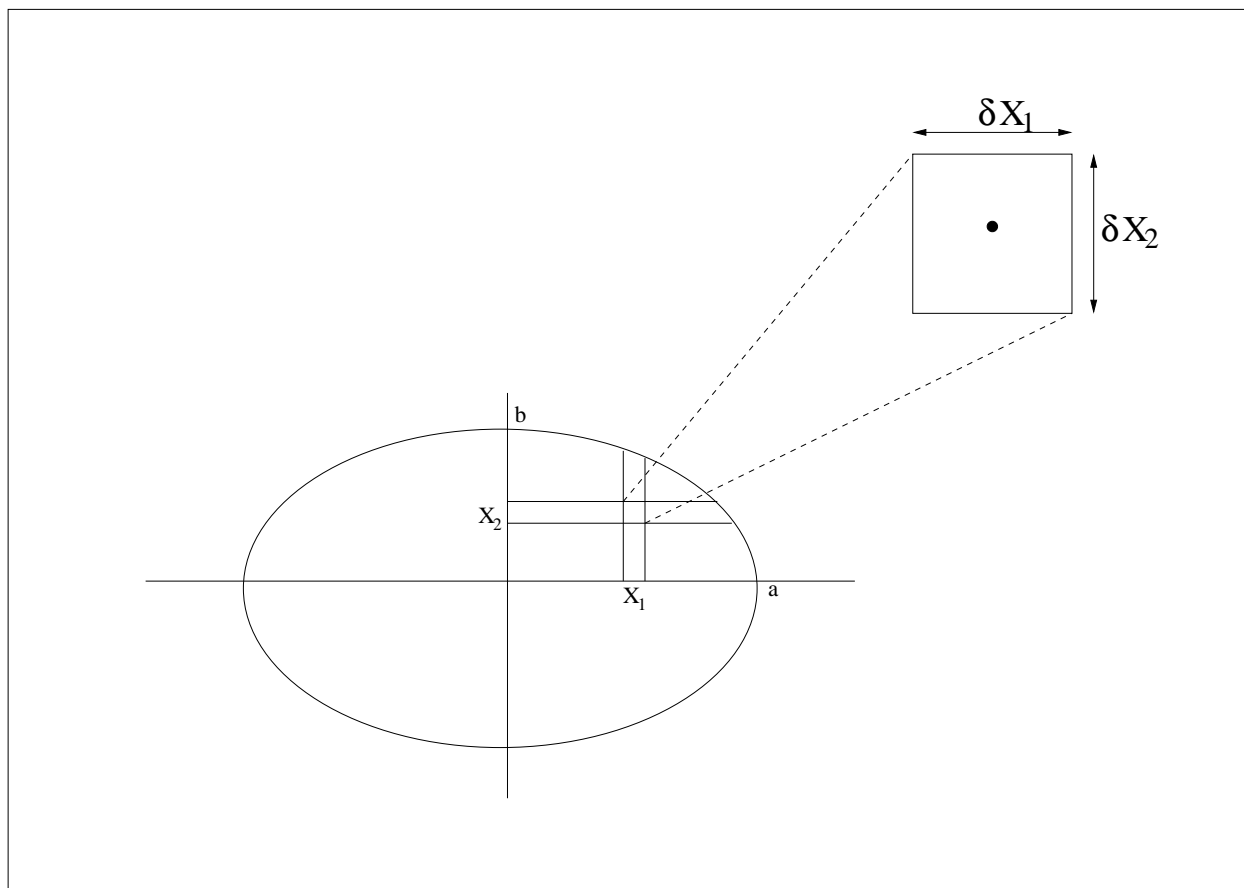


Figure 4

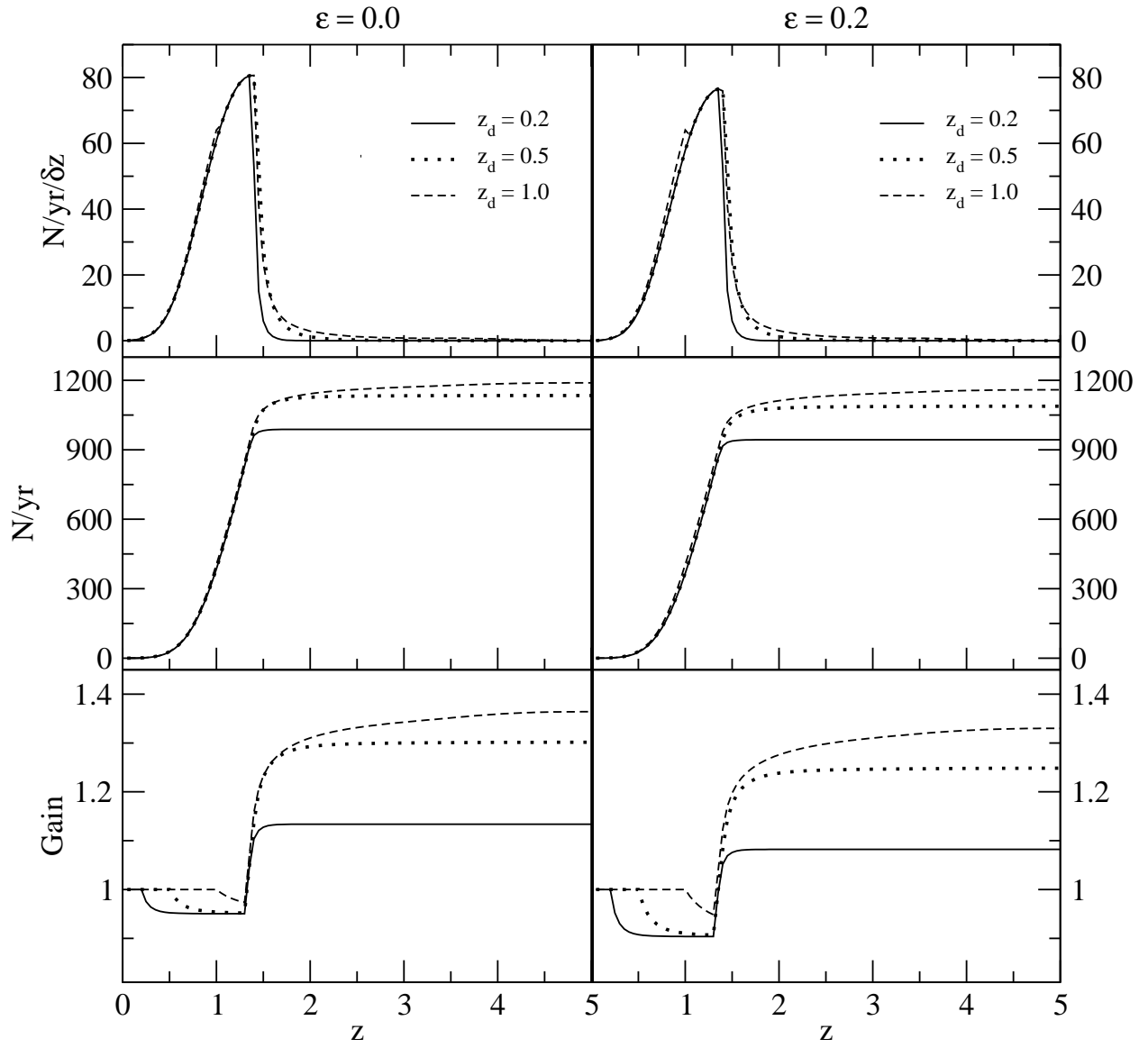


Figure 5

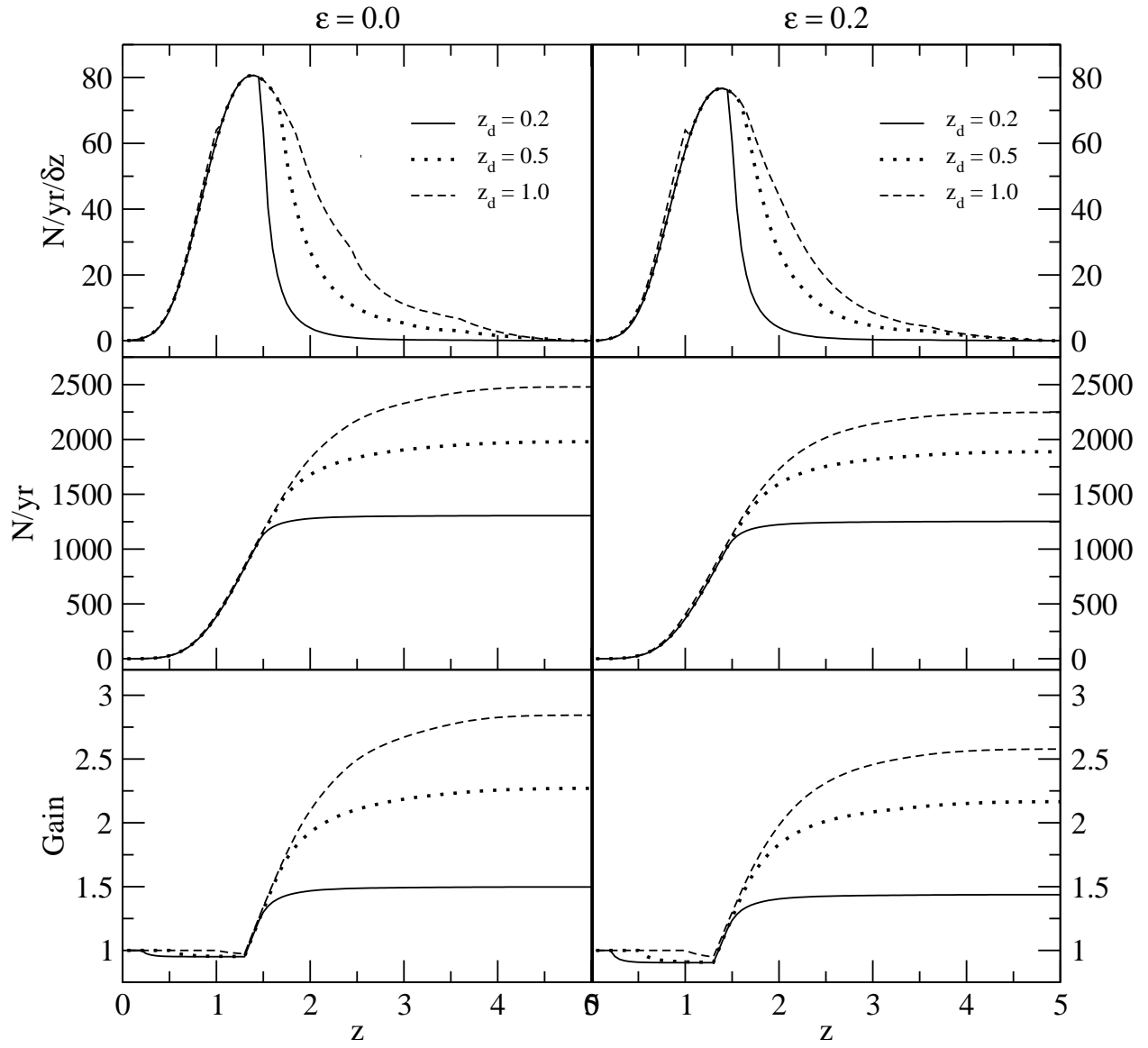


Figure 6

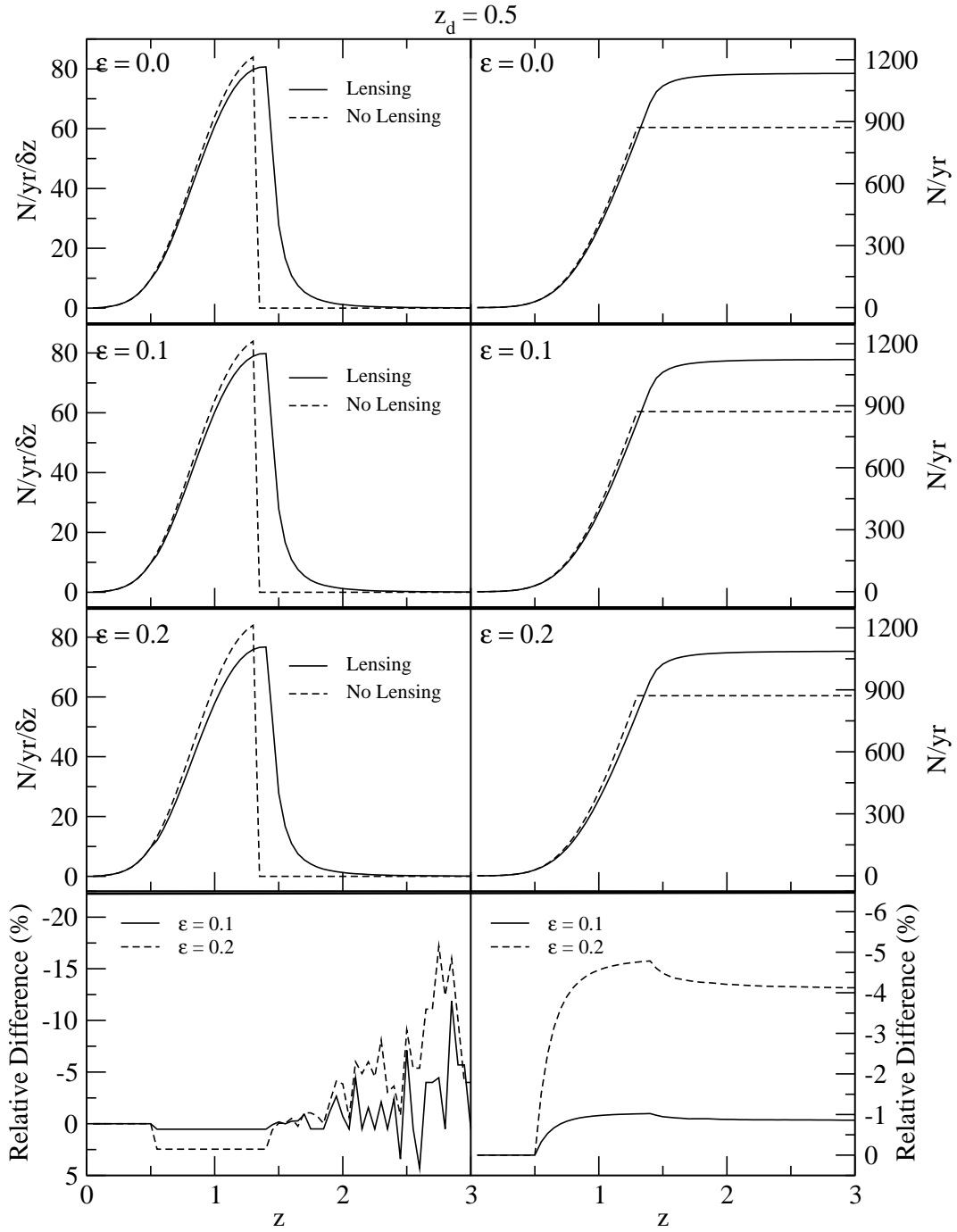


Figure 7

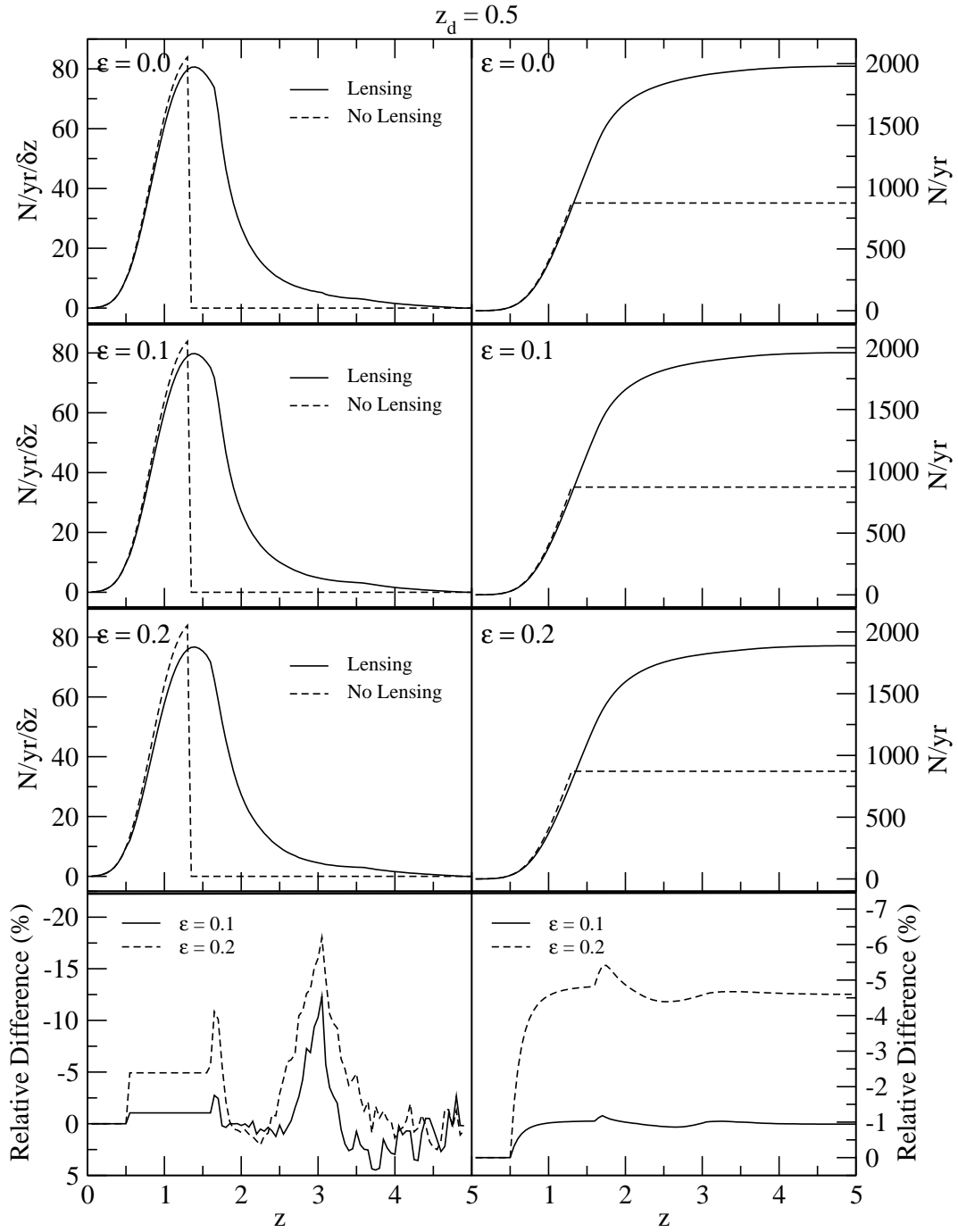


Figure 8

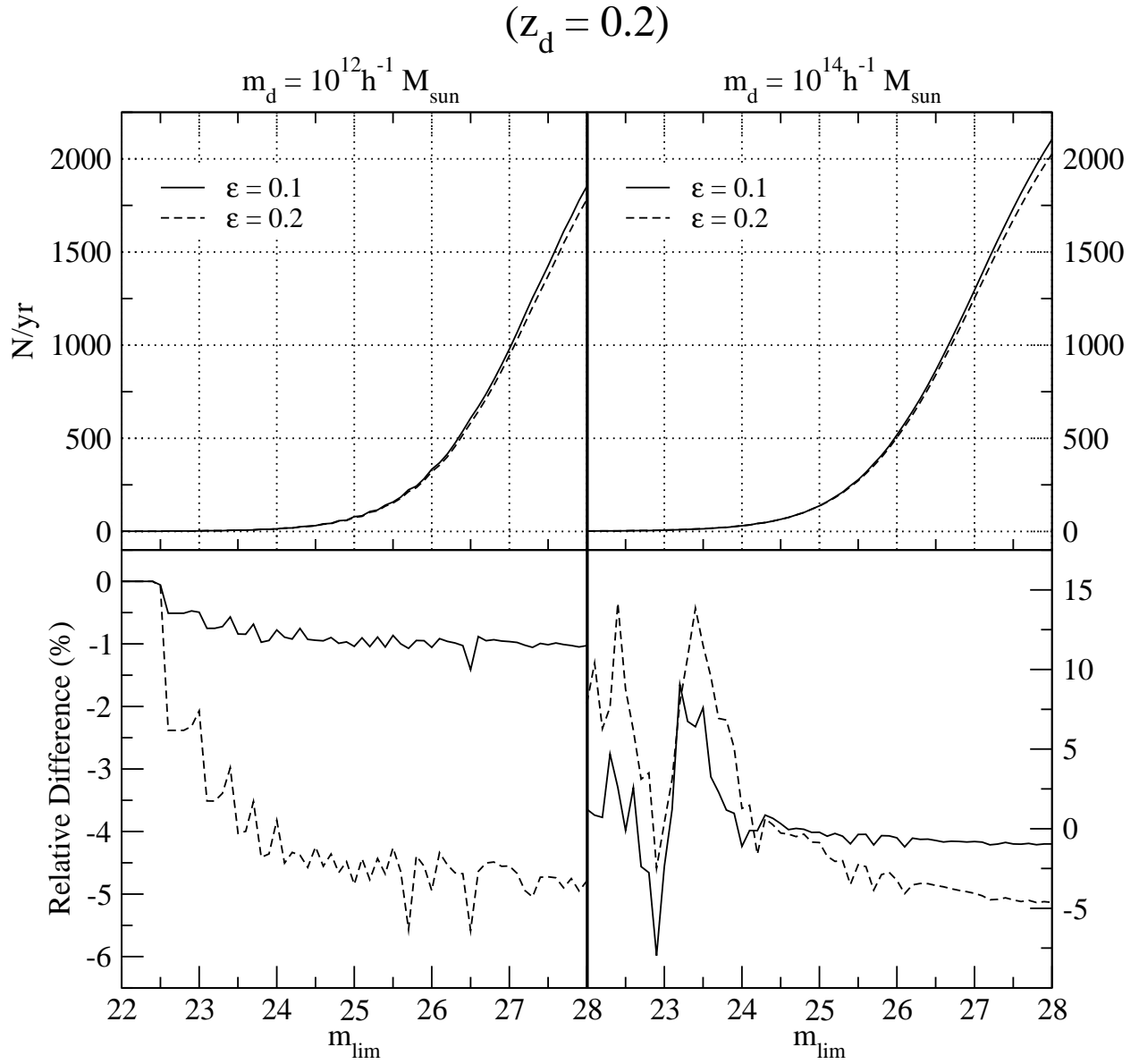


Figure 9

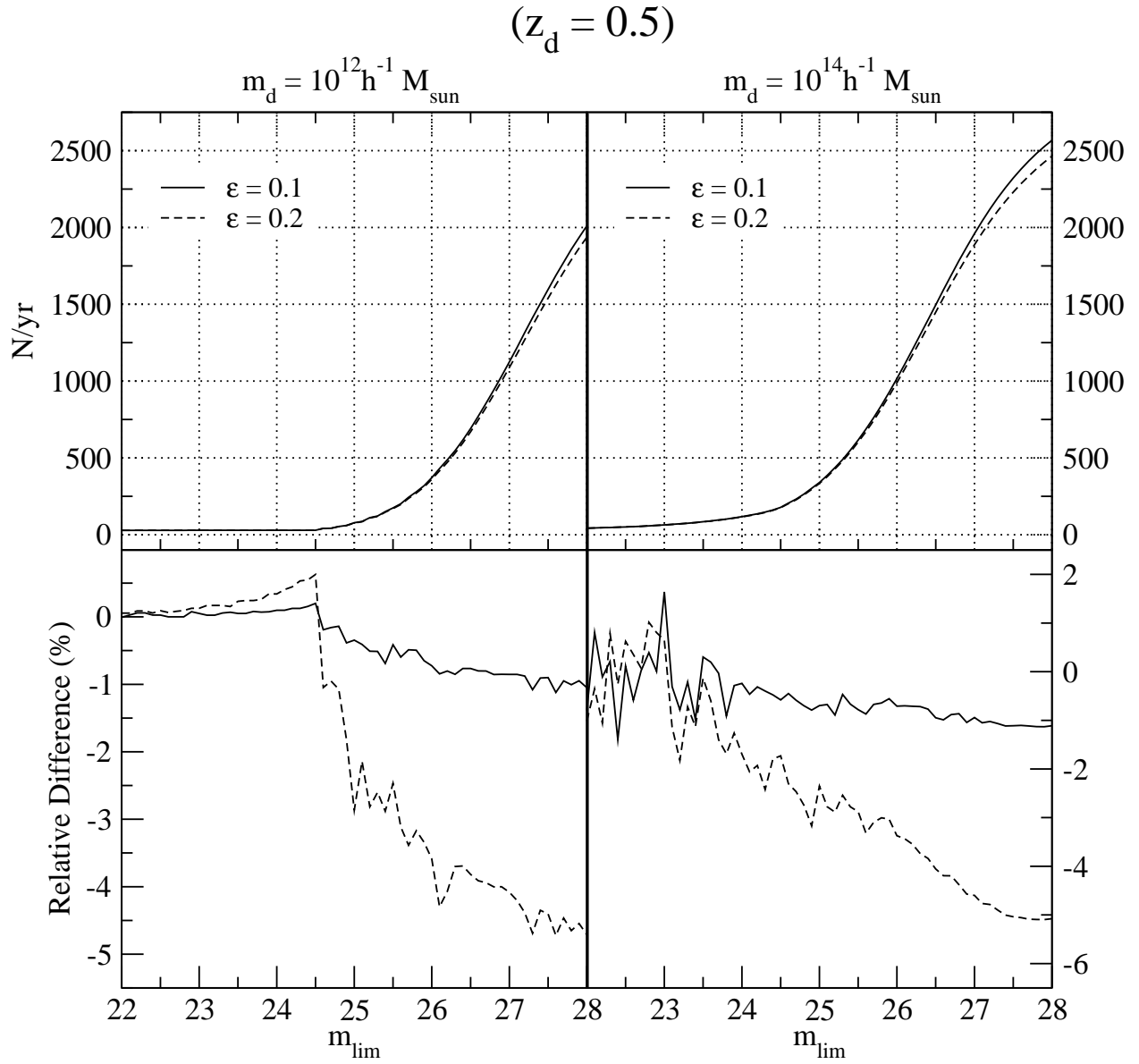


Figure 10

($z_d = 1.0$)

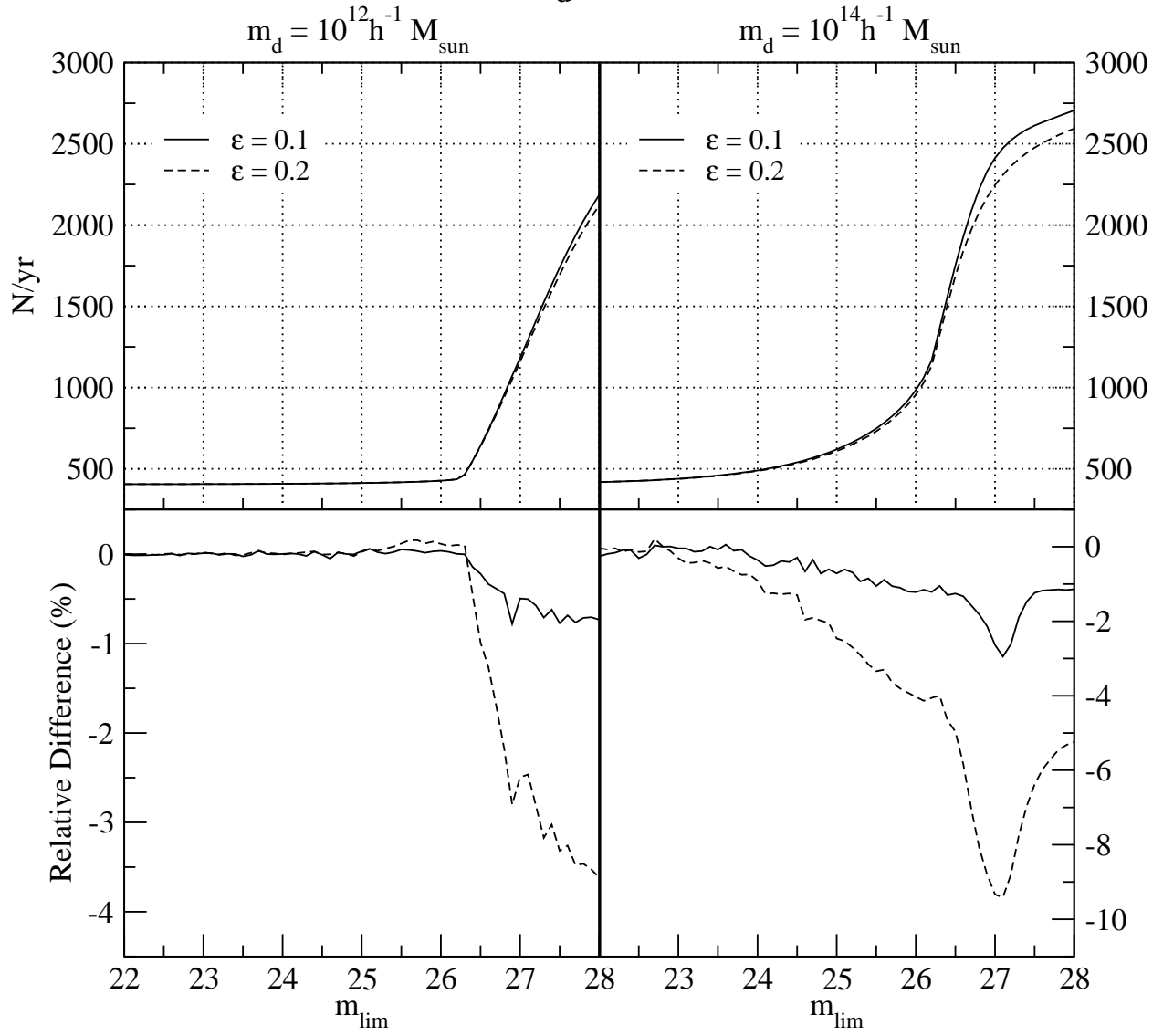


Figure 11